

Assessment of High-Temperature Oxidation Properties of 316L Stainless Steel Powder and Sintered Porous Supports for Potential Solid Oxide Cells Applications

Ahsanul Kabir^{1,2*}, Damian Koszelow¹, Tadeusz Miruszewski³,
Victor Buratto Tinti⁴, Vincenzo Esposito⁴, Frank Kern², Sebastian Molin¹

¹ Faculty of Electronics, Telecommunications, and Informatics, Gdańsk University of Technology, Gabriela Narutowicza 11/12, 80-233 Gdańsk, Poland

² Institute for Manufacturing Technology of Ceramic Components and Composites, University of Stuttgart, 70569 Stuttgart, Germany

³ Institute of Nanotechnology and Materials Engineering, Faculty of Applied Physics and Mathematics, Gdańsk University of Technology, ul. Gabriela Narutowicza 11/12, 80-233 Gdańsk, Poland

⁴ Department of Energy Conversion and Storage, Technical University of Denmark, 2800 Kgs Lyngby, Denmark

* Corresponding author's e-mail: sebastian.molin@pg.edu.pl

ABSTRACT

In this work, the oxidation properties of austenitic 316L stainless steel powder and sintered porous support were investigated at the temperature range of ~600–750 °C for 100 hours in ambient air. Oxidation kinetics was determined by continuous thermogravimetry and analyzed employing parabolic rate law. It was observed that oxidation leads to the formation of an oxide scale, with substantial oxidation occurring at ≥ 650 °C in the powder. The porous steel support was fabricated using the tape casting method with two distinct pore former concentrations. The microstructural features of both the powder and support were investigated by X-ray diffractometry and scanning electron microscopy coupled with energy-dispersive X-ray analysis. The mechanical properties of the metal support were examined before and after oxidation via a microhardness test. The effect of porosity on the resulting properties of the metal support was also highlighted. In summary, 316L stainless steel support suits SOCs applications below 600 °C.

Keywords: 316L stainless steel, high-temperature oxidation, XRD, microstructure, porosity.

INTRODUCTION

Porous stainless steel, as a supporting component for solid oxide cells (SOCs), has grown significantly over the last decade. Stainless steel used as support brings several key advantages over conventional ceramic forms (electrolyte and fuel electrode), such as high thermal/electronic conductivity, mechanical ruggedness, redox stability, excellent tolerance to fast start-up, and ease of manufacturing [1, 2, 3]. Additionally, it enables employing much thinner ceramic functional layers, resulting in less polarization resistance as well as low material and operational cost,

ultimately paving the way for widespread application prospects of SOCs [4]. For the SOCs application, a high level of porosity (between 30 and 40 vol%) is required in the steel support for the gas permeation. Thus, a very high specific surface area is exposed to air in the SOCs operating temperature range of 600–800 °C [3, 5]. These conditions will inevitably cause the porous steel to oxidize [6] and induce the evolution of protective oxide scales (Cr_2O_3 , chromia) around the steel particles, which fill up the pore space and restrict gas transport [7]. Subsequently, the electronic conductivity and mechanical properties of steel decrease, leading to long-term degradation of cell

performance [8]. In addition to the oxidation, Cr can evaporate as CrO_3 and $\text{CrO}_2(\text{OH})_2$ under oxidizing atmospheres, possibly poisoning the SOC electrodes and reducing their electrochemical activity [9]. It was found that in stainless steel with a high chromium content, the oxide scale ideally grows following the parabolic Wagner/Pilling-Bedworth relation due to diffusion control and the low oxygen diffusivity in the scale, protecting the underlying steel from further oxidation [10]. However, if the oxidation rate is very high, the chromium content within the steel alloy depletes significantly, which will cause the development of a non-protective oxide scale, such as Fe_2O_3 . This process, known as breakaway oxidation (cracking and spalling), eventually shortens the lifespan of the steel component [11]. Generally, the oxidation rate is sensitive to the chemical composition of steel (mainly chromium level), exposure temperature, gas atmosphere, moisture level, and the porosity of the support, with higher porosity producing higher mass gain based on the superficial surface area [12, 13]. By studying the oxide growth rate parameters, the lifetime limit of the steel can be predicted [14].

Ferritic stainless steels are widely applied as standard material for metal support in SOCs applications, including 430L, 70Fe30Cr, Crofer22 APU, Cr26Fe ITM, and ZMG232 [15, 16, 17]. Their high-temperature oxidation behaviors are well-examined in porous and powder forms [9] [18]. Furthermore, to the best of authors' knowledge, little attention was paid to the oxidation behavior of austenitic stainless steel and its possible application feasibility in SOCs. In the current



work, the high-temperature oxidation properties of an austenitic 316L stainless steel were investigated in both powder and sintered porous structured form. Studying raw powder with a high surface-to-volume ratio can provide new insights into oxidation parameters and be used as a model system for sintered porous steels, especially to predict the upper limit of oxidation temperature and possible lifespan. The parabolic rate law is employed to estimate the rate constant (k_p) and activation energy (E_a) of oxidation in the powder from 600 °C to 750 °C in air. On the basis of the obtained data from the powder, the oxidation temperature of the sintered porous support is selected. The effect of porosity on the oxidation, microstructural, and mechanical properties of the support is emphasized.

Experimental procedures

The material used in this work is a commercial austenitic AISI 316L stainless-steel powder (Sandvik, Sweden), with a specific surface area of 0.11 m^2/g as obtained via BET analysis. The planar porous support was produced using the conventional tape-casting method. Two slurries were prepared with different solid loadings and pore former amounts. The slurry composition is shown in Table S1. The green tape was dried at room temperature for 24 hours and debound at 550 °C for 2 hours with a slow heating/cooling ramp of 0.5 °C min^{-1} . Finally, the tape samples were sintered in a tubular furnace in a pure H_2 atmosphere at 1250 °C for 2 hours. The high-temperature oxidation test was performed by continuous thermogravimetric measurement using a custom-made thermobalance (CI

Table 1. Tape casting recipe of the 316L stainless steel sheet (weight percentage)

Parameter	Steel powder	Rice starch	PVA	Glycerin	PEG-6000	Water	Defoamer
Support 1	66.30	9	15.15	2.2	0.5	6.6	0.25
Support 2	59.70	12	15.8	3.6	0.6	8.0	0.30

Green tape		Support 1		Support 2
------------	---	-----------	--	-----------

Precision MK5-G2) between 600–750°C (for the powder) and 600 °C (for the support) with a heating rate of 10 °C min⁻¹ in flowing air (40 ml · min⁻¹) for 100 hours. The crystallographic phase composition was analyzed by X-ray diffraction (XRD) using a Philips PANalytical X’Pert Pro system (Germany) containing CuKα1 radiation ($\lambda = 1.542 \text{ \AA}$) within the 2θ range from 20–80°. The sampling steps were 0.01° 2θ and the scanning speed was 0.0185°/second. A high-resolution scanning electron microscope (Thermo Fisher Phenom XL-SEM) coupled with an energy-dispersive X-ray spectrometer was used to evaluate the morphology and microstructure of samples. The mechanical properties of the samples (fresh and oxidized) were investigated using a Vickers LECO LM700 micro-indentation (Leitz, Metallux, Germany) unit equipped with an optical microscope. Measurements were carried out with a standard trapezoidal load-hold-unload cycle, with a loading/unloading rate of ~5 mN/s. The hold time was 10 s at a maximum load

of 98 mN. The elastic modulus was calculated from the initial slope of the unload-displacement curve using the Oliver-Pharr method [19].

RESULTS AND DISCUSSION

The SEM image of the surface of the as-received 316L steel powder (without any further sieving) is presented in Figure 1a. This powder is loosely agglomerated and has a spherical shape, typical for gas-atomized powder. The mean particle size is ca. 5 μm (Figure 1b). As it can be observed, the surface of the powder is relatively clean and shows no presence of oxide particulates. XRD analysis illustrates that the powder is mainly comprised of a face-centered cubic austenite phase (γ) with a minor presence of a body-centered cubic (BCC) ferrite phase (α). The chemical composition of the powder is presented in Table S2. The powders were isothermally oxidized at a high

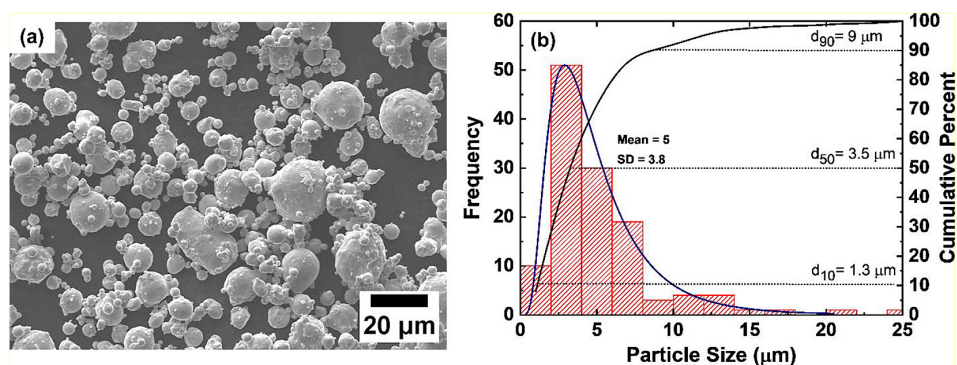
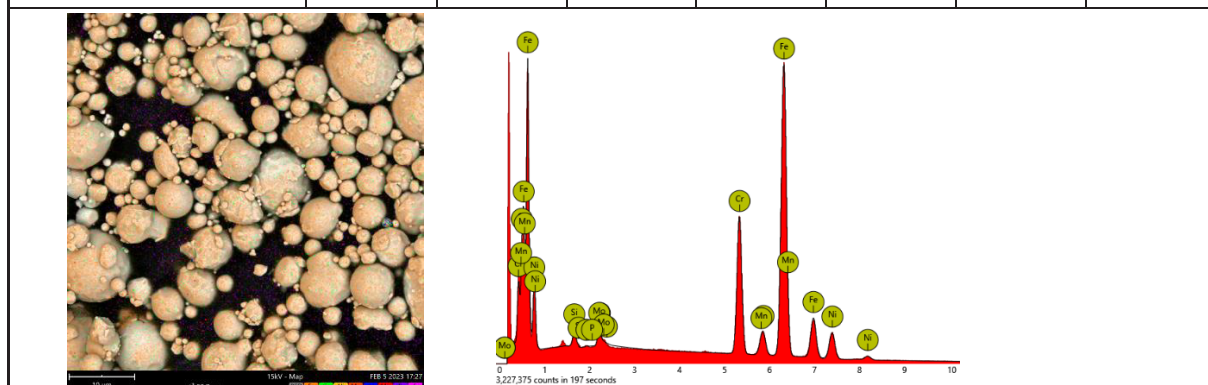


Figure 1. (a) SEM image of the as-received 316L stainless steel powder and (b) corresponding particle size distribution histogram, as measured from the micrograph and lognormal fitting (blue solid line)

Table 2. Chemical composition of the 316L powder, as determined from SEM-EDS (performed with a magnification of 5000×) analysis and manufacturer data (weight percentage)

Parameter	Si	Mo	Ni	Cr	Mn	P	Fe
As received	0.67	1.49	9.67	17.10	1.85	0.01	69.20
Manufacturer data	0.5–1.0	2.0–3.0	12.0–14.0	16.0–18.0	0.2	-	Bal.



temperature of $\sim 600\text{--}750\text{ }^\circ\text{C}$ for 100 hours, and the mass gain results are plotted in Figure 2a. Similar to the previously published reports, it was assumed that the powder has a constant specific surface area during oxidation [18][20]. At $600\text{ }^\circ\text{C}$, the mass gain is rather low. Nonetheless, the mass gain is tremendously pronounced with increasing exposure temperatures, with the most significant growth occurring at $750\text{ }^\circ\text{C}$. After 100 h of measurements, the specific mass gain of the powder oxidized at $600\text{ }^\circ\text{C}$ was $0.028\text{ mg}\cdot\text{cm}^{-2}$, whereas, at $750\text{ }^\circ\text{C}$, it was $0.25\text{ mg}\cdot\text{cm}^{-2}$, which is roughly 9 times higher than the former. The data is also represented in relative mass change unit (%) in Figure 1. Relative mass change is a useful parameter and is frequently used in literature, which indicates how much oxygen has been taken up in the oxide scale growth. As shown in Figure 1, the powder oxidized at $650\text{ }^\circ\text{C}$ exhibited a mass gain above 15%, which is 15 times higher than that of authors' previous studies for 430L powder (average size of

$75\text{ }\mu\text{m}$) [18]. Such a substantial difference points out the combined role of stainless-steel composition and surface area for oxidation properties. The corrosion rate constant is estimated employing the Pilling-Bedworth equation, as shown below:

$$\left(\frac{\Delta m}{A}\right)^{1/n} = k_p t + C \quad (1)$$

where: $\Delta m/A$ – the mass change per unit surface area ($\text{mg}\cdot\text{cm}^{-2}$), t is the time of oxidation in seconds and k_p is the parabolic rate law constant ($\text{g}^2\cdot\text{cm}^{-4}\cdot\text{s}^{-1}$). C represents the integration constant that defines the onset of parabolic kinetics.

It is worth mentioning that the n value, i.e., the degree of deviation index, which is generally 0.5, deviates from the parabolic law $\geq 650\text{ }^\circ\text{C}$. At temperatures of $650\text{--}750\text{ }^\circ\text{C}$, the oxidation shows an initial parabolic regime followed by breakaway-type kinetics (accelerated regime). A recent study by Huang et al. on 316L dense steels reported

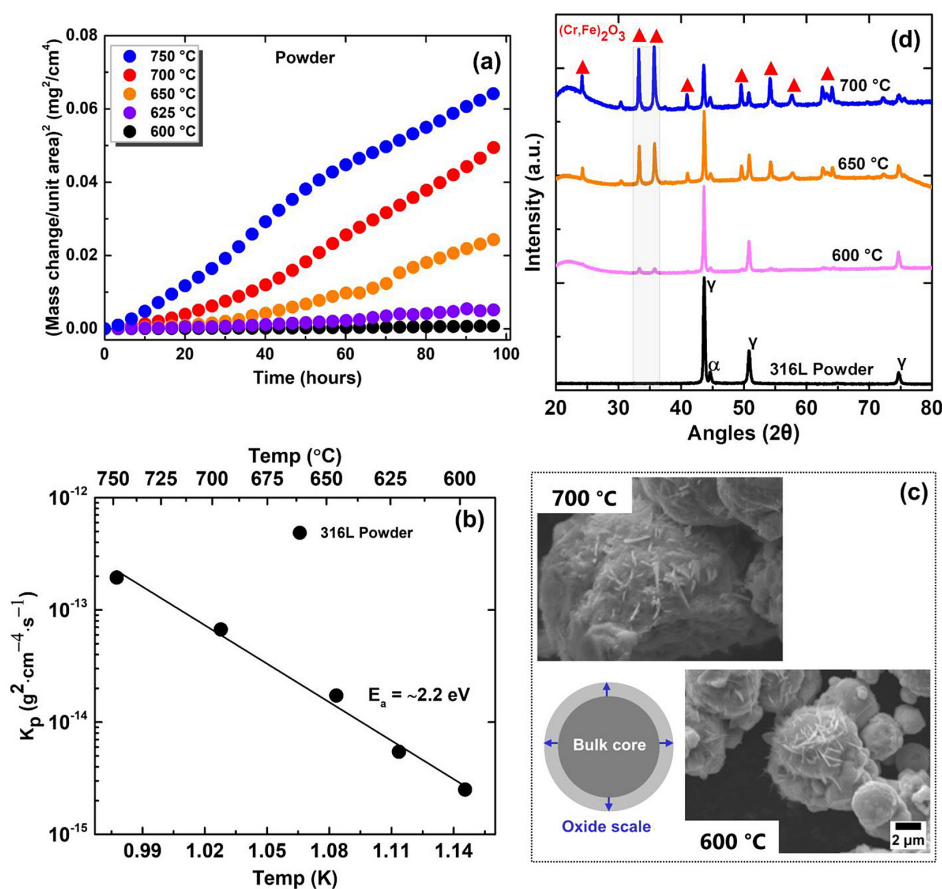


Figure 2. (a) Oxidation kinetics of 316L steel powder at a temperature of $600\text{--}750\text{ }^\circ\text{C}$, plotted as a square of mass change with respect to the initial specific surface area against oxidation times. (b) Arrhenius plot of the parabolic oxidation rate constant as a function of inverse temperature. (c) SEM image (15000x) of the 316L oxidized powder exposed to air for 100 hours, and (d) XRD patterns of 316L steel (fresh) and (oxidized) powders

similar results and hypothesized that such deviation is due to different diffusion coefficients of O, Cr, Fe, and Ni through the oxide films at various oxidation temperatures [21]. At low temperatures, thinner oxide film causes elements to diffuse out more easily, leading to the appearance of parabolic oxidation kinetics. In contrast, at high temperatures the spalling of oxides (breakaway oxidation) will create a new surface to form new oxides so that the surface layers no longer constrain the oxidation. This effect would dramatically increase the oxidation rate and improve the diffusion rate of elements during the oxidation process [22]. Thus, fitting is performed at the initial stage of the test i.e. below 30 hours for the sample oxidized at 650–750 °C. From the fitting, the parabolic rate constant k_p is calculated. The temperature-dependent k_p is plotted in a function of inverse temperature (T), shown in Fig. 2b, following the Arrhenius relationship,

$$k_p = k_0 \exp\left(\frac{-E_a}{kT}\right) \quad (2)$$

where: k_0 is the pre-exponential factor, E_a is the activation energy of oxidation, and k is the Boltzmann constant.

The estimated activation energy of oxidation is ~2.2 eV, consistent with the reported value for 430L powders [18] but a slightly low value for chromia film growth [23]. The activation energy of Cr diffusion in Cr_2O_3 is around 2.9 eV [6]. The possible reasons for reduced activation energy are the small variations of the scale chemical composition or simultaneous oxidation of iron, which has a lower value. In comparison to the ferritic 430L alloy, the corrosion rate of 316L powder is around two orders of magnitude higher at 700 °C.

Figure 2c illustrates the surface morphologies of the oxidized powder exposed to air for 100 hours. As it can be seen, the oxide particles have a needle/flake-like morphology with sharp edges. The number of oxide crystallites progressively increased along with oxidation temperature, and the oxide layer grew thicker, with average sizes exceeding 1–3 μm . The results of chemical analysis performed using the EDS method (Fig. 2) and phase analysis from the XRD measurement (Fig. 2d) postulated that the oxides are enriched with Cr_2O_3 and Fe_2O_3 . It should be noted that according to the Cr_2O_3 - Fe_2O_3 phase diagram, these oxides form a solid solution in the investigated temperature range; thus, diffracted phase reflection is indexed with general form as a $(\text{Fe,Cr})_2\text{O}_3$ [16]. In the air, these oxides are thermodynamically stable. The intensity of the $(\text{Fe,Cr})_2\text{O}_3$ phase is increased along with temperature. This effect occurs because, at high-temperature (≥ 650 °C), 316L steel is prone to intergranular corrosion, which proceeds by forming the chromium-depleted regions and subsequently would initiate breakaway oxidation, i.e. deterioration of the protective Cr_2O_3 layer [16]. The $(\text{Fe,Cr})_2\text{O}_3$ peaks also shift towards a lower 2-theta value at higher temperatures, highlighting particle size coarsening. Within the resolution limit of XRD, no secondary phases of Mn-Cr spinel or SiO_2 are found in any of the oxidized samples.

The sintering of the tape-cast 316L support was performed under dry H_2 at 1250 °C for 2 hours. The porosity of the support has been optimized by controlling the parameters, including pore former content, sintering temperature, sintering time, etc., to achieve high porosity (see Fig. 3–7) and adequate mechanical strength. The

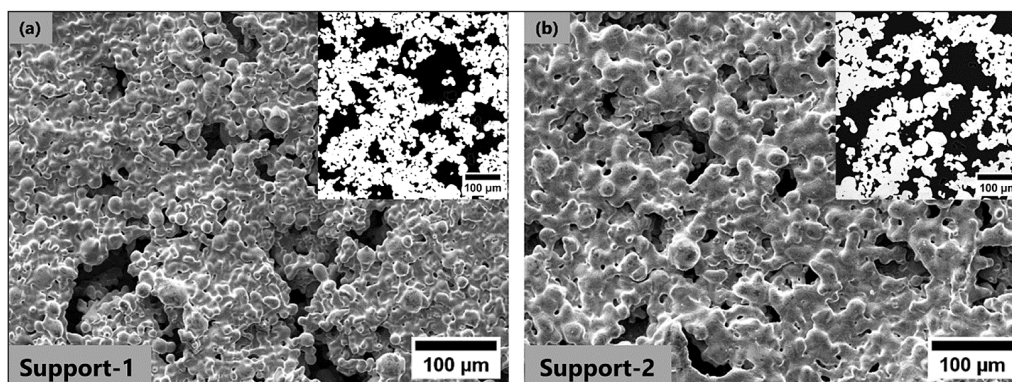


Figure 3. Surface and polished (inset) cross-sectional micrographs of the metal supports, sintered at 1250 °C for 2 hours in pure H_2 (a) Support 1: 9 wt.% pore former content and (b) Support 2: 12 wt.% pore former content. Image magnification: 600x (inset)

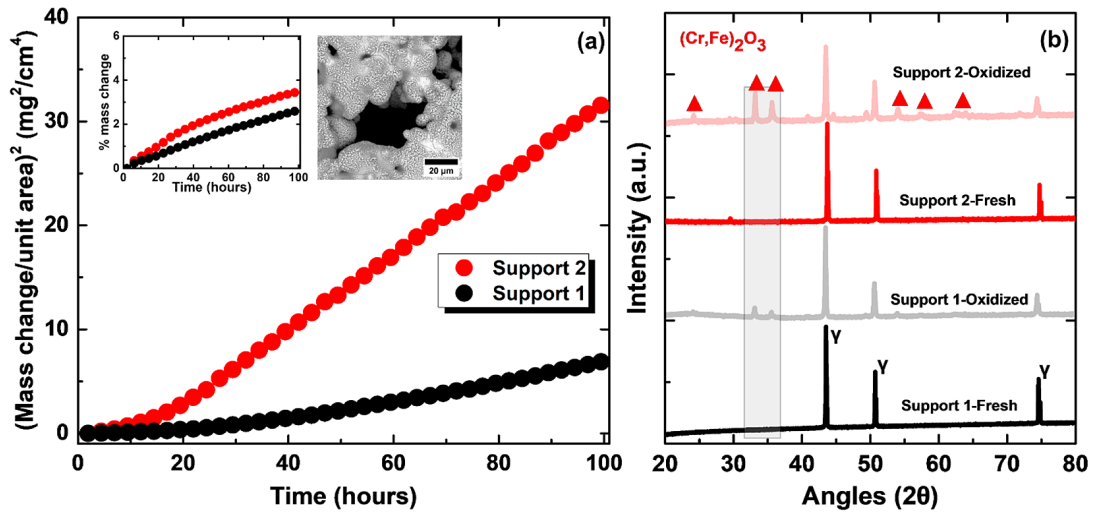


Figure 4. (a) Oxidation kinetics of porous metal support at a temperature of 600 °C, plotted as a square of mass change per unit area against oxidation times. (Inset) percentage of mass change against oxidation times and surface SEM image after oxidation (support-2). (b) XRD patterns of the fresh and oxidized (600 °C for 100 hours) metal support

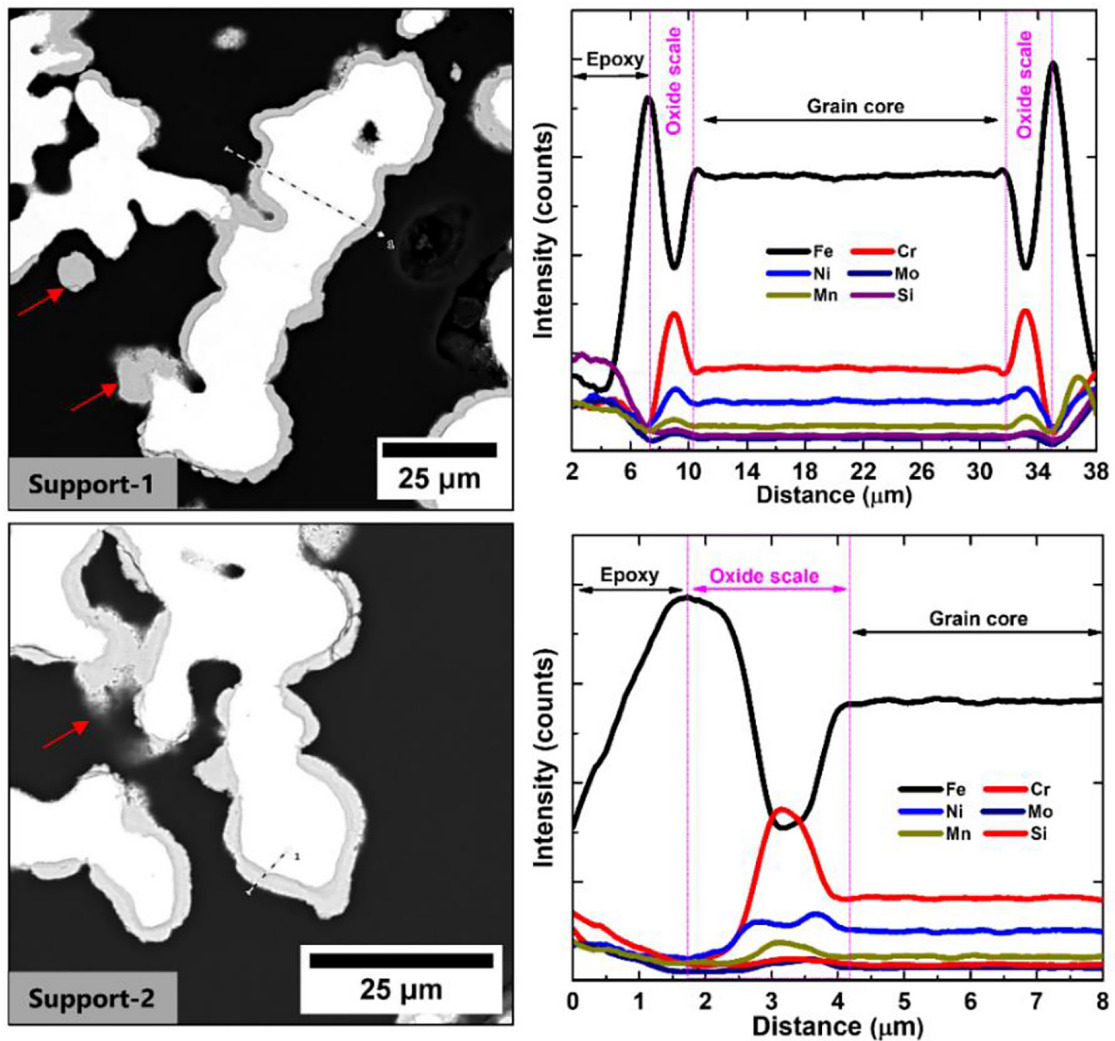


Figure 5. SEM cross-section images and EDS analysis of the metal support after oxidation at 600 °C in air, (a) Support 1: 9 wt.% pore former content and (b) Support 2: 12 wt.% pore former content

surface and polished cross-sectional microstructure of the sintered support are illustrated in Figure 3. As it can be observed, the steel particles are well percolated, and sintering necks between the particles are formed. The average grain size lies between 15–20 μm . There is no sponge-like layer developed, and the pores have finger-like geometry. Small pores, as well as large pores of ~ 80 μm in diameter, can be seen. The porosity of the support, as measured using the ImageJ software, is in the range of 40–50%, which is in line with the desired porosity for MS-SOCs.

Taking into account the powder oxidation data, the chosen oxidation temperature for the as-sintered porous support was 600 $^{\circ}\text{C}$, and the subsequent oxidation kinetic results are displayed in Figure 4a. For the case of the sintered support with a low specific surface area (< 0.02 $\text{m}^2 \cdot \text{g}^{-1}$), the measurement of the specific surface area is problematic (instrumental limitation of BET analysis) [18]. Therefore, the data was calculated considering the superficial geometric area of the sample. It can be seen that the relative mass gain is similar to the powder, and oxidation kinetics is parabolic. The sample with higher porosity (Support-2) demonstrates higher mass gain. This result is expected because of the more residual porous area accessible for oxidation. Within the parabolic regime, the oxide scale is expected to be crack-free and protect the substrate from further oxidation. After 100 h of oxidation in air, supports 1 and 2 gained ~ 2.6 and 3.5% of the initial mass (fresh sample), respectively. Figure 4b shows the XRD pattern of the fresh and oxidized sintered support. As it was noted, the peak corresponding to oxide $(\text{Cr,Fe})_2\text{O}_3$

is found where the intensity of the peak is significantly higher in support 2 than in support 1, further confirming more oxidation in support-2.

Visual inspections of the post-oxidized samples demonstrate a clear change in color from grey to dark grey/black. The surface becomes rough and is covered with a finely structured oxide scale, covering most of the grains and grain boundaries (inset Figure 4a). It partially filled many of the pore spaces between the grains and thus reduced the porosity of the sample. The SEM image of the polished cross-sectional structures in Figure 5 and Figure S8–S9 displays the formation of visible oxide scales around the grain core. The scale is shown to have both large-scale and very small-scale structures. They seem to adhere continuously to the grains with barely any shattering in the cross-section and mostly have continuous coverage. The average thickness of the oxide layers is estimated to be between 1–3 μm , which is below the threshold value of 3 μm thickness for estimating the lifespan of the alloy, as proposed by Tucker et al. [24]. However, a large thickness (≥ 5 μm) and isolated scales were also observed in a few locations. The EDS analysis of the oxidized sample was composed of higher O concentration than fresh samples, as it can be seen in Fig. S8. The EDS line-scan depth profiles across the thickness of oxide layers in Figure 5 and the EDS point-scan in Figure 9 illustrate the depletion of Fe and accumulation of Cr, Ni, and Mn occurring in the oxide scale. However, the exact composition is difficult to quantify due to the inherent limitation of the EDS method, pore abnormalities, and irregular scale thickness.

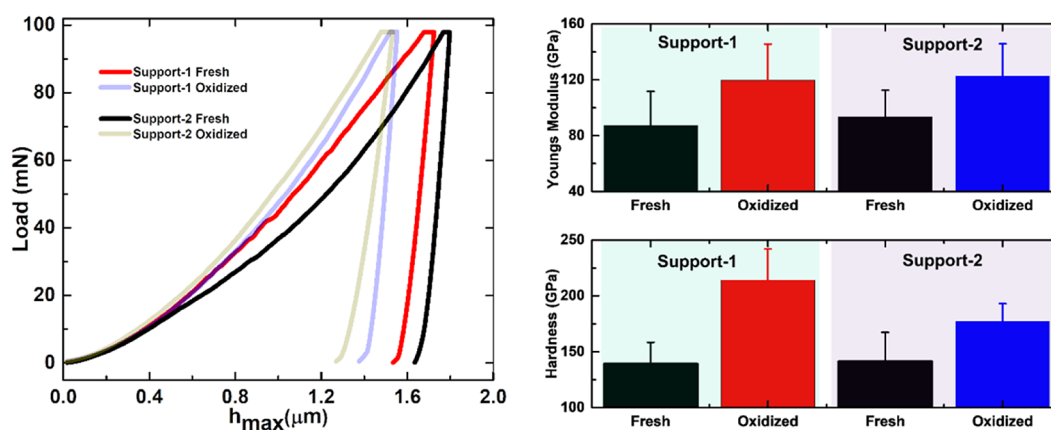


Figure 6. (a) Typical load-displacement curves and (b) Microhardness and elastic modulus of the fresh and oxidized (600 $^{\circ}\text{C}$ for 100 hours) metal supports. The standard deviation indicates the high reproducibility of the tests with a coefficient of variation of 10–15 % of the mean

The oxide scales are protective, as also confirmed by mechanical analysis (see Fig. 6). It was measured that the oxidized sample has higher microhardness and elastic modulus than the fresh samples. At the maximum load of 98 mN, the maximum penetration depth of the oxidized sample was 1.4 μm for the support-1 and 1.5 μm for the support-2, indicating a higher indentation resistance of the $(\text{Cr,Fe})_2\text{O}_3$ scale that conceivably delays the onset of non-protective oxidation as a consequence. Likewise, in other metallic alloys, as reported in Ref [25], steel allows oxygen to be dissolved beneath the oxide scale in the support, resulting in a rise in hardness in the oxidized sample. As estimated, both the support demonstrates identical hardness in the fresh state. However, after thermal oxidation support 1 demonstrates a higher hardness increment than support-2. It was also observed that the hardness value decreased steadily as the distance from the oxide contacts. It should be noted that the properties measured from the oxidized sample reflect a combination of the properties of the oxide scale and substructure (fresh-state). The stress in oxide scales is usually in a compressive state caused by (i) “thermal stress” associated with the mismatch of thermal expansion between the oxide scales and metallic substrate and (ii) oxide “growth stresses” that develop during its growth at oxidation temperature [26, 27]. The elastic recovery is 0.17 μm and 0.25 μm for support-1 and support-2 respectively, suggesting similar elastic deformation for each oxide layer during indentation.

CONCLUSIONS

The oxidation behavior of austenitic 316L stainless steel powder and sintered porous support were evaluated in this paper. The high-temperature oxidation in the powder follows the parabolic rate law at low temperatures, showing a strong deviation at ≥ 650 °C. The observed oxide scale was $(\text{Fe,Cr})_2\text{O}_3$, as evaluated using XRD and SEM-EDS analyses. For the sintered porous support, oxidation is enhanced with increased porosity. The oxide scale is continuous with an average thickness of 1–3 μm and shows no cracking. The oxidized sample has higher mechanical properties than fresh steel, suggesting its protective nature. In summary, the presented results highlight that a 316L stainless steel support is suitable for long-term operating temperatures ≤ 600 °C.

Acknowledgments

This project was supported by National Science Centre Poland (NCN) Sonata Bis 8 project number 2018/30/E/ST8/00821 “High-temperature corrosion studies and development of oxidation lifetime model of alloy powders and sintered porous alloys: effects of composition and microstructure”.

REFERENCES

1. Tucker M.C. Development of High power density metal-supported solid oxide fuel cells, *Energy Technology* 2017; 5(12): 2175–2181, doi: 10.1002/ente.201700242.
2. Dogdibegovic E., Wang R., Lau G.Y., and Tucker M.C. High performance metal-supported solid oxide fuel cells with infiltrated electrodes, *J Power Sources* 2019; 410–411: 91–98, doi: 10.1016/j.jpowsour.2018.11.004.
3. Reiser M., Berova V., Aphale A., Singh P., and Tucker M.C. Oxidation of porous stainless steel supports for metal-supported solid oxide fuel cells, *Int J Hydrogen Energy* 2020; 45(55): 30882–30897, doi: 10.1016/j.ijhydene.2020.08.015.
4. Stange M., Denonville C., Larring Y., Haavik C., Brevet A., Montani A., Sicardy O., Mougín J., Larsson P.-O. Coating developments for metal-supported solid oxide fuel cells, *ECS Trans* 2013; 57(1): 511–520, doi: 10.1149/05701.0511ecst.
5. Zhou Z., Nadimpalli V.K., Pedersen D.B., and Esposito V. Degradation mechanisms of metal-supported solid oxide cells and countermeasures: A review, *Materials* 2021; 14(11): 3139, doi: 10.3390/ma14113139.
6. Stefan E., Denonville C., Larring Y., Stange M., and Haugrud R. Oxidation study of porous metal substrates for metal supported proton ceramic electrolyzer cells, *Corros Sci* 2020; 164: 108335, doi: 10.1016/j.corsci.2019.108335.
7. Koszelow D., Molin S., Karczewski J., Marone F., and Makowska M. Morphology changes in Fe-Cr porous alloys upon high-temperature oxidation quantified by X-ray tomographic microscopy, *Mater Des* 2022; 215: 110492, doi: 10.1016/j.matdes.2022.110492.
8. Zhou Z., Nadimpalli V.K., Lalwani A.R., Wang S., Shang Y., Pan Z., Pedersen D.B., Esposito V. Oxidation inhibition of 3D printed porous steel by ceria-activated multilayers, *Corros Sci* 2023; 214, 111010, doi: 10.1016/j.corsci.2023.111010.
9. Molin S., Kusz B., Gazda M., and Jasinski P. Evaluation of porous 430L stainless steel for SOFC operation at intermediate temperatures, *J*

- Power Sources 2008; 181(1): 31–37, doi: 10.1016/j.jpowsour.2007.10.009.
10. Huntz A.M. Arabolic laws during high temperature oxidation: relations with the grain size and thickness of the oxide,” *J Mater Sci Lett* 1999; 18(24): 1981–1984, doi: 10.1023/A:1006677631548.
 11. Karczewski J., Dunst K.J., Jasinski P., and Molin S. High temperature corrosion and corrosion protection of porous Ni22Cr alloys, *Surf Coat Technol* 2015; 261: 385–390, doi: 10.1016/j.surfcoat.2014.10.051.
 12. Molin S., Gazda M., and Jasinski P. High temperature oxidation of porous alloys for solid oxide fuel cell applications, *Solid State Ion* 2010; 181(25–26): 1214–1220, doi: 10.1016/j.ssi.2010.06.049.
 13. Koszelow D., Makowska M., Drewniak A., Cempura G., Jasiński P., and Molin S. High-temperature Corrosion of ~30 Pct Porous FeCr Stainless Steels in Air: Long-Term Evaluation Up to Breakaway, *Metallurgical and Materials Transactions*, 2023, doi: 10.1007/s11661-023-07005-z.
 14. Koszelow D., Makowska M., Marone F., Karczewski J., Jasiński P., and Molin S. High temperature corrosion evaluation and lifetime prediction of porous Fe22Cr stainless steel in air in temperature range 700–900 °C, *Corros Sci* 2021; 189: 109589, doi: 10.1016/j.corsci.2021.109589.
 15. Drewniak A., Koszelow D., Błaszczak P., Górnicka K., Jurak K., Javed H., Sabato A.G., Jasiński P., Molin S., Smeacetto F. Glass-ceramic sealants and steel interconnects: Accelerated interfacial stability and reactivity tests at high temperature,” *Mater Des* 2021; 212: 110259, doi: 10.1016/j.matdes.2021.110259.
 16. Molin S., Gazda M., Kusz B. and Jasinski P. Evaluation of 316L porous stainless steel for SOFC support, *J Eur Ceram Soc* 2009; 29(4): 757–762, doi: 10.1016/j.jeurceramsoc.2008.07.027.
 17. Palcut M., Mikkelsen L., Neufeld K., Chen M., Knibbe R., and v. Hendriksen P. Corrosion stability of ferritic stainless steels for solid oxide electrolyser cell interconnects, *Corros Sci* 2010; 52(10): 3309–3320, doi: 10.1016/j.corsci.2010.06.006.
 18. Karczewski J., Brylewski T., Miruszewski T., Andersen K.B., Jasinski P.Z., and Molin S. High-temperature kinetics study of 430L steel powder oxidized in air at 600–850 °C, *Corros Sci* 2019; 149: 100–107, doi: 10.1016/j.corsci.2019.01.005.
 19. Oliver W.C. and Pharr G.M. An improved technique for determining hardness and elastic modulus using load and displacement sensing indentation experiments, *J Mater Res* 1992; 7(6): 1564–1583, doi: 10.1557/JMR.1992.1564.
 20. Chyrkin A., Schulze S.L., Pirón-Abellán J., Bleck W., Singheiser L., and Quadackers W.J., Oxidation limited lifetime of ni-base metal foams in the temperature range 700–900 °C, *Adv Eng Mater* 2010; 12(9): 873–883, doi: 10.1002/adem.201000139.
 21. Huang X., Xiao K., Fang X., Xiong Z., Wei L., Zhu P., Li X. Oxidation behavior of 316L austenitic stainless steel in high temperature air with long-term exposure, *Mater Res Express* 2020; 7(6): 066517, doi: 10.1088/2053-1591/ab96fa.
 22. Robertson J. and Manning M.I. Limits to adherence of oxide scales, *Materials Science and Technology* 1990; 6(1): 81–92, doi: 10.1179/mst.1990.6.1.81.
 23. Sabioni A.C.S., Huntz A.-M., da Luz E.C., Mantel M., and Haut C. Comparative study of high temperature oxidation behaviour in AISI 304 and AISI 439 stainless steels, *Materials Research* 2003; 6(2): 179–185, doi: 10.1590/S1516-14392003000200012.
 24. Tucker M.C. Progress in metal-supported solid oxide electrolysis cells: A review, *Int J Hydrogen Energy* 2020; 45(46): 24203–24218, doi: 10.1016/j.ijhydene.2020.06.300.
 25. Ahmed F.S., El-Zomor M.A., Ghazala M.S.A., and Elshaer R.N. Effect of oxide layers formed by thermal oxidation on mechanical properties and NaCl-induced hot corrosion behavior of TC21 Ti-alloy, *Sci Rep* 2022; 12(1): 19265, doi: 10.1038/s41598-022-23724-6.
 26. Pascal C., Braccini M., Parry V., Fedorova E., Mantel M., Oquab D., Monceau D. Relation between microstructure induced by oxidation and room-temperature mechanical properties of the thermally grown oxide scales on austenitic stainless steels, *Mater Charact* 2017; 127: 161–170, doi: 10.1016/j.matchar.2017.03.003.
 27. Simms H.G. Oxidation Behaviour Of Austenitic Stainless Steels At High Temperature In Supercritical Plant, 2011.